Supplementary Information (SI) for Catalysis Science & Technology.

Electronic Supplementary Information (ESI)

The Effect of Organic Ligand Skeletons of 2D π–d Conjugated Metal-organic Frameworks on their OER Performance and Stability

Xiaolong Yang[a, b], Haoqiang Ai*[b], Zheng Cui*[b], Xiaohan Song[b], Yuanyuan Liu[c], Baibiao Huang*[c], Huixuan Wang[d], Danning Xing*[b]

[a] Institute of Thermal Science and Technology, Shandong University, Shandong 250100, P. R. China

[b] Shandong Institute of Advanced Technology, Shandong 250100, P. R. China

[c] State Key Lab of Crystal Materials, Shandong University, Shandong 250100, P. R. China

[d] The First Affiliated Hospital of Shandong First Medical University, Shandong 250100, P. R. China

E-mail: haoqiang.ai@iat.cn; zhengc@iat.cn; bbhuang@sdu.edu.cn; danning.xing@iat.cn

Synthesis CoTHT and FeTHT electrocatalysts.

CoTHT: Firstly, under argon atmosphere, 0.075 mmol of cobalt acetylacetonate ($Co(acac)_2$) was dissolved in 50 mL of CH_2Cl_2. Separately, 0.05 mmol of 2,3,6,7,10,11-triphenylenehexathiol (THT) was dissolved in 40 mL of NH_4OH aqueous solution (0.1 mol L^{-1}) under argon atmosphere and ultrasonication. Inside a glovebox, a pure NH_4OH aqueous solution (10 mL, 0.1 mol L^{-1}) was gently layered on top of the CH_2Cl_2 solution to form a liquid-liquid interface. Subsequently, the THT solution was slowly injected to the aqueous phase. The reaction vessel was sealed and left undisturbed under argon for 5 days. A black film was formed at the liquid-liquid interface gradually. The resulting film was collected as a powder, which underwent solvent exchange with water (3 × 20 mL) and ethanol (3 × 20 mL). The final product was vacuum-dried for further analysis.

FeTHT: Firstly, under argon atmosphere, 0.075 mmol of iron acetylacetonate ($Fe(acac)_2$) was dissolved in 50 mL of CH_2Cl_2. Separately, 0.05 mmol of 2,3,6,7,10,11-triphenylenehexathiol (THT) was dissolved in 40 mL of NH_4OH aqueous solution (0.1 mol L^{-1}) under argon atmosphere and ultrasonication. Inside a glovebox, a pure NH_4OH aqueous solution (10 mL, 0.1 mol L^{-1}) was gently layered on top of the CH_2Cl_2 solution to form a liquid-liquid interface. Subsequently, the THT solution was slowly injected to the aqueous phase. The reaction vessel was sealed and left undisturbed under argon for 5 days. A black film was formed at the liquid-liquid interface gradually. The resulting film was collected as a powder, which underwent solvent exchange with water (3 × 20 mL) and ethanol (3 × 20 mL). The final product was vacuum-dried for further analysis.

Characterization

The scanning electron microscopy (SEM) images were obtained using a TESCAN MIRA LMS device from the Czech Republic. The synchrotron X-ray diffraction (sXRD) patterns were collected at beamline BL14B1 of the Shanghai Synchrotron Radiation Facility (SSRF) using X-rays with an energy of 18 keV. The morphology and microstructure of the materials were observed with a FEI Talos F200x 200 kV transmission electron microscope (TEM). X-ray photoelectron spectroscopy (XPS) data were collected on a Thermo Scientific K-Alpha spectrometer. Fourier-transform infrared (FTIR) spectra were recorded using a Thermo Fisher Scientific Nicolet iS20 instrument. Raman spectra were obtained at a laser wavelength of 532 nm using a Renishaw in Via system. The Brunauer-Emmett-Teller (BET) surface area analysis was conducted at liquid nitrogen temperature using a Micromeritics ASAP Kubo X1000 analyzer. The elemental content of metals in the materials was determined by inductively coupled plasma optical emission spectroscopy (ICP-OES) on a PerkinElmer Optima 8300 instrument.

The Co K-edge and Fe K-edge X-ray absorption spectroscopy (XAS) of the products were measured at the 1W1B beam line of the Beijing Synchrotron Radiation Facility (BSRF) using transmission mode. The Extended X-ray Absorption Fine Structure (EXAFS) data were collected through a fixed-exit double-crystal Si (111) monochromator. The EXAFS raw data were processed using standard procedures in the ATHENA program, including background subtraction, normalization, and Fourier transformation. The EXAFS $\chi(k)$ data were subsequently fitted and analyzed using the ARTEMIS program.

Electrochemical characterizations

Electrochemical experiments were conducted using a three-electrode system in 1 M KOH solution by a CHI 760E electrochemical workstation. The graphite rod was used as the counter electrode and Ag/AgCl electrode served as the reference electrode. The carbon cloth (CC) loaded with catalysts were employed as the working electrode. All the samples were examined at a scan rate of 10 mV s^{-1}, and the potential was calibrated to the reversible hydrogen electrode (RHE) using the equation E(RHE) = E(Ag/AgCl) + 0.197 + 0.059 pH. All the polarization curves were subjected to IR compensation to correct for ohmic losses. The electrochemical active surface area (ECSA) of the samples were obtained through cyclic voltammetry (CV) curves in the non-Faradaic region at different scan rates. Electrochemical impedance spectroscopy (EIS) of the samples was performed at a voltage of 1.7 V (vs. RHE), within the frequency range of 0.1 Hz to 100 kHz. The stability of FeCoTHT and FeCoBHT was evaluated using chronoamperometry method in 1.0 M KOH aqueous solution at 1.55 V (vs. RHE) over a duration of 15 hours. The O_2 generation experiment was tested in an airtight electrolytic cell using chronopotentiometry at a voltage of 1.7 V (vs. RHE).

The calculation formula for Faradaic Efficiency is shown as follows:

$$FE = \frac{M}{\frac{Q}{1.6 \times 10^{-19} \times n \times R}} \times 100\% \tag{1-1}$$

Where:

M is the actual oxygen evolution amount in moles (mol); Q is the total transferred charge in coulombs (C), in this case, 71.52 C; n is the number of electrons transferred during the OER process, which is $4e^-$; R is Avogadro's constant, 6.02×10^{23} mol^{-1}; $1.6\times10^{-19}$is the charge of one electron in coulombs (C). The oxygen yield of FeCoTHT within 60 minutes was measured to be 183.55 μmol, and the calculated Faradaic efficiency was calculated close to 100%.

The ECSA is calculated using the following formula:

$$ECSA = \frac{C_{dl}}{C_s} \tag{1-2}$$

Where:

C_{dl} is the double-layer capacitance of the catalyst obtained by fitting the CV curves, as shown in Fig. 7d, and C_s is the specific capacitance per unit area, The C_s varies depending on factors such as electrode material and electrolyte composition.

Theoretical calculations

Our spin-polarized density functional theory (DFT) calculations were implemented in the Vienna Ab initio Simulation Package[1,2]. The projector augmented wave pseudo-potentials method[3] and the generalized gradient approximation in the form of Perdew–Burke–Ernzerhof (PBE)[4] were employed. To describe the Coulomb and exchange interactions of the strongly localized d electrons, PBE + U calculations were conducted. Based on prior studies[5], an effective Hubbard U_{eff} value of 3.0 eV was used for transition-metal atoms. A vacuum region of approximately 15 Å in the vertical direction was introduced to prevent interactions between periodic slabs. The plane-wave basis set was truncated at a cutoff energy of 400 eV. Convergence criteria were set at 10^{-6} eV for energy and 0.03 eV $Å^{-1}$ for forces. Van der Waals (vdW) interactions were addressed using the DFT-D3 method[6]. The 2×2×1 and 4×4×1 Γ-centered Monkhorst-Pack[7] *k*-point sampling were used for structure optimization and energy calculations, respectively. Charge transfer between transition-metal atoms and ligands was analyzed using Bader's approach[8]. The Atomic Simulation Environment[9] was utilized for visualizing atomic structures.

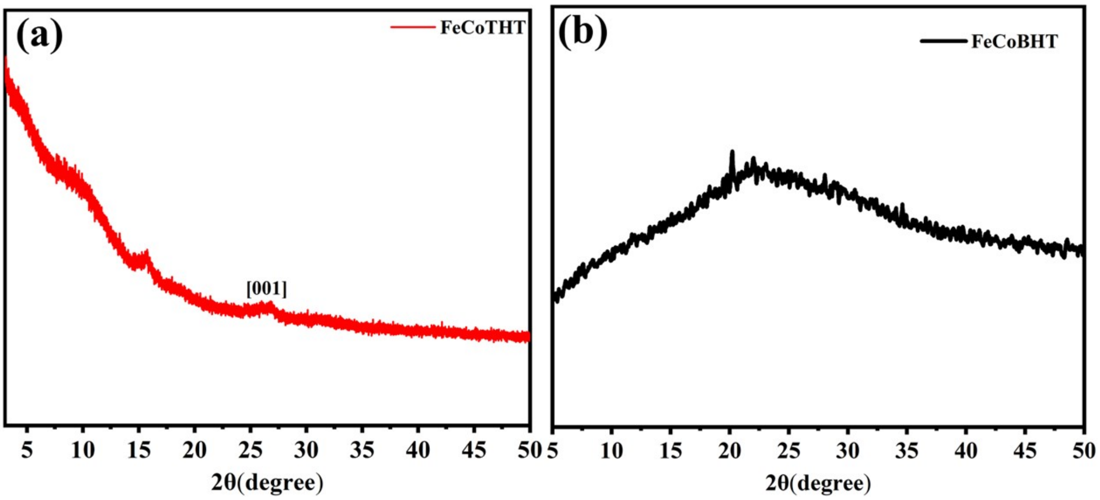

Fig. S1 XRD profiles of (a) FeCoTHT and (b) FeCoBHT. The XRD pattern reveals distinct peaks for FeCoTHT at 2θ = 15.5° and 26.6°, indicating a well-defined crystalline structure. In contrast, FeCoBHT shows no prominent crystalline peaks, confirming its amorphous nature. This observation aligns with previous reports on similar materials[10].

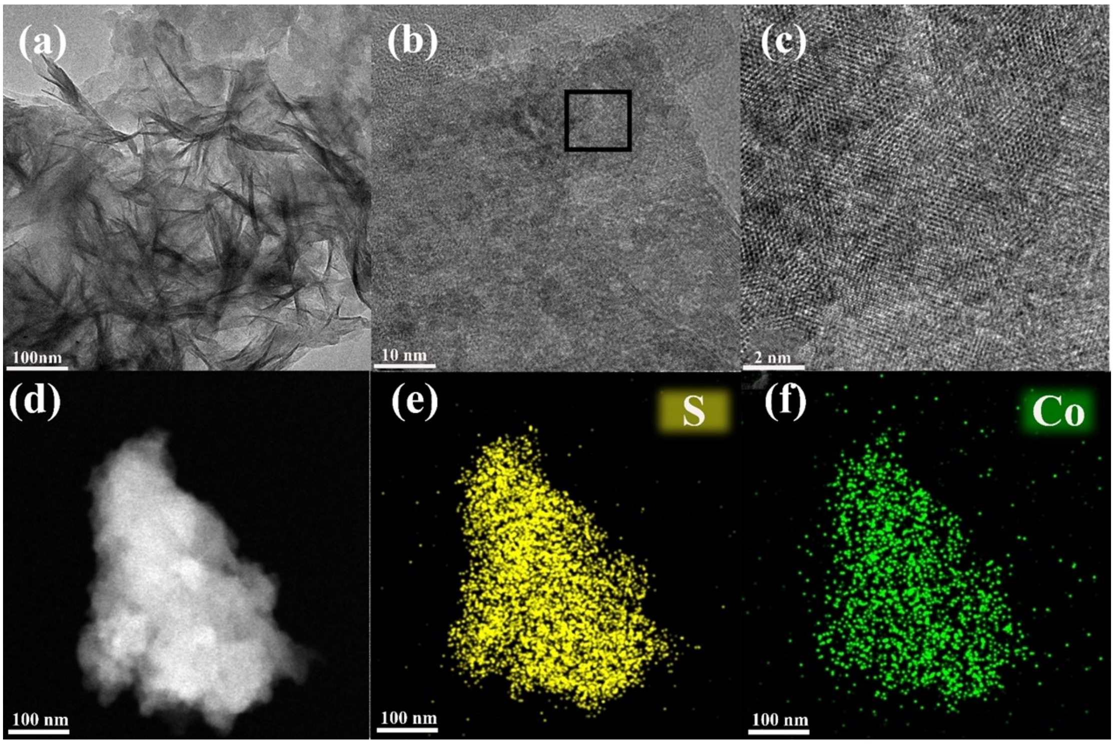

Fig. S2 (a) TEM, (b) HRTEM, (c) magnified HRTEM image for the black box in b and (d) HAADF-STEM of CoTHT, (e-f) EDX element mapping of CoTHT, yellow points for S in (e), green points for Co in (f).

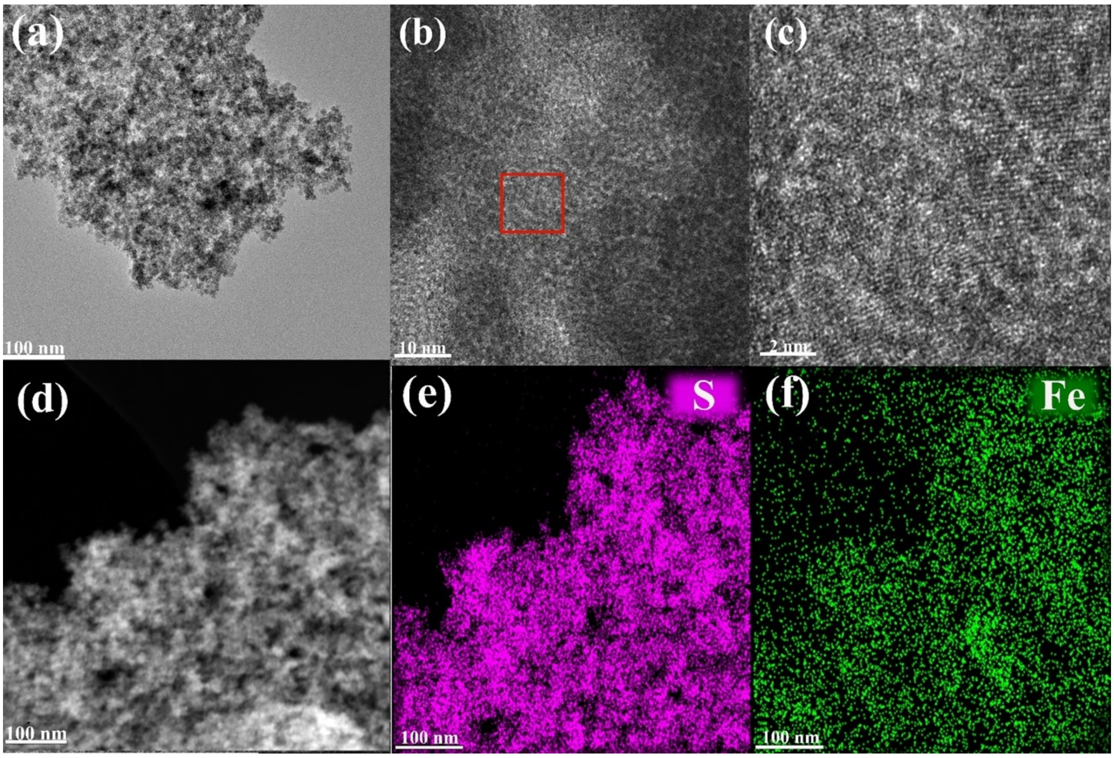

Fig. S3 (a) TEM, (b) HRTEM, (c) magnified HRTEM image for the red box in b and (d) HAADF-STEM of FeTHT, (e-f) EDX element mapping of FeTHT, purple points for S in (e), green points for Fe in (f).

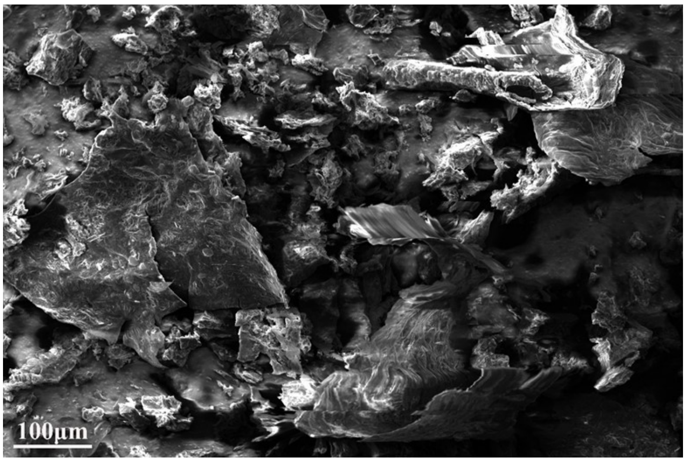

Fig. S4 SEM images of FeCoBHT. The morphology of FeCoBHT in the figure clearly shows a sheet-like structure, consistent with previous related reports[10].

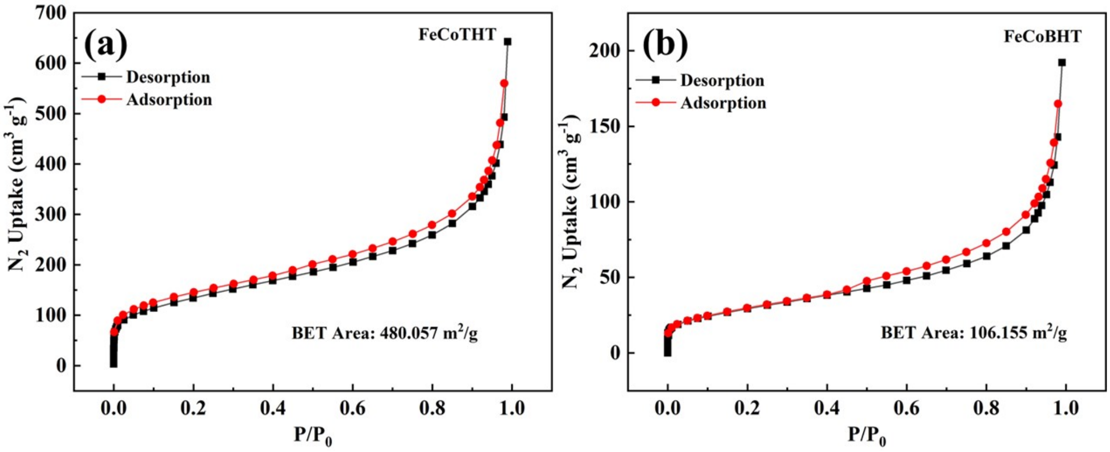

Fig. S5 N_2 adsorption−desorption isotherms of (a) FeCoTHT and (b) FeCoBHT.

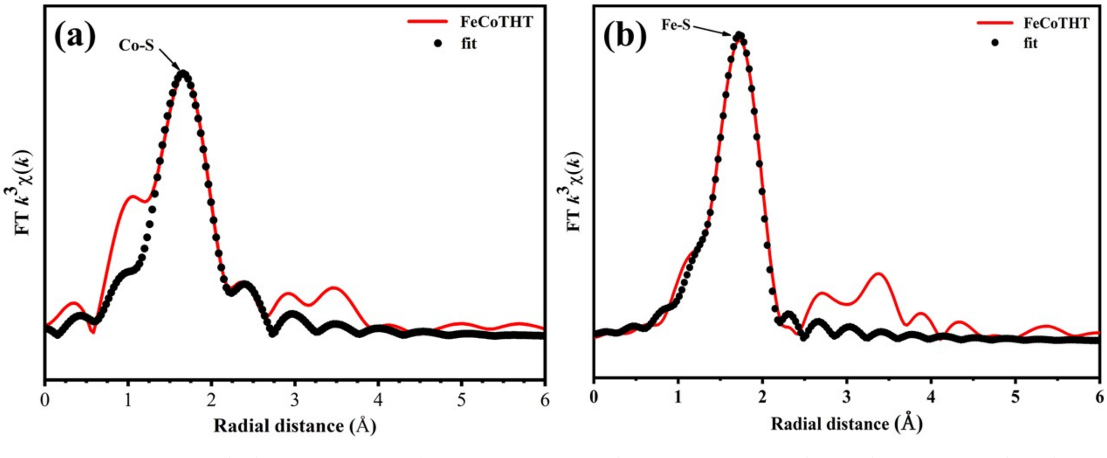

Fig. S6 EXAFS fitting curves of FeCoTHT at the (a) Co K-edge, (b) Fe-K edge in R space.

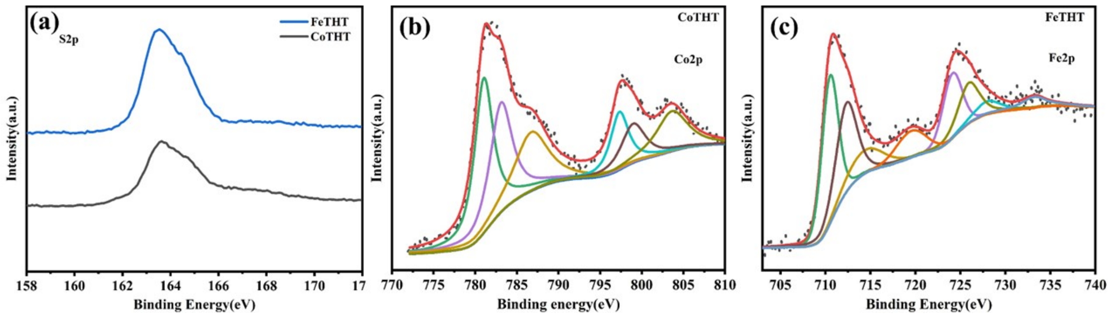

Fig. S7 XPS spectra: (a) S 2p spectra of CoTHT and FeTHT; (b) Co 2p spectrum of CoTHT and (c) Fe 2p spectrum of FeTHT. The S 2p peak positions for FeTHT and CoTHT match well with that of FeCoTHT, indicating a strong interaction between THT and the metal elements. The analysis the Fe 2p and Co 2p spectra of FeTHT and CoTHT confirms that both Fe and Co are in a mixed +2/+3 oxidation state, which is consistent with the results for FeCoTHT.

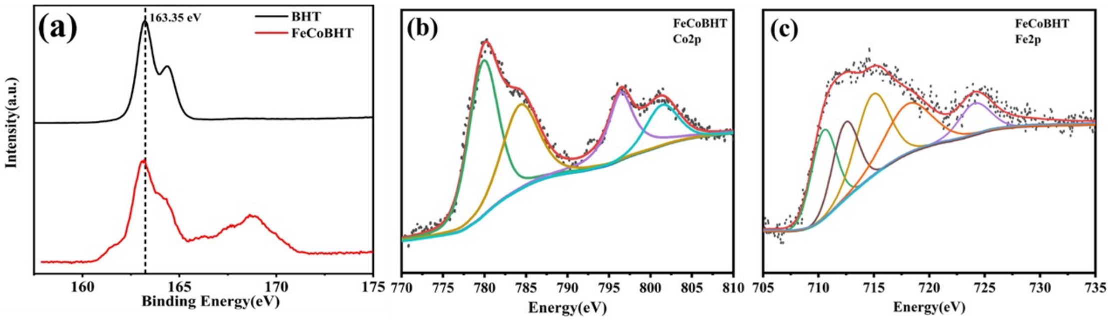

Fig. S8 XPS (a) S 2p of FeCoBHT and BHT; Co 2p (b) and Fe 2p (c) spectra of FeCoBHT.

The S 2p peak of FeCoBHT at 163.22 eV is attributed to the characteristic signal of the S-C bond[11]. Compared with BHT (163.35 eV), the S-C peak of FeCoBHT exhibits a 0.13 eV shift toward a lower binding energy, indicating the electron accumulation on the sulfur atoms and confirming the interaction between the metal ions and the BHT ligands. The result demonstrates the strong electronic interaction between the metal ions and the BHT ligand. Additionally, the peak at 168.73 eV in FeCoBHT corresponds to the S-O bond, suggesting partial oxidation of sulfur species during the synthesis process.

The Co 2p spectrum of FeCoBHT can be deconvoluted into four peaks, with binding energies at 780.20 eV and 796.50 eV corresponding to the Co $2p_{3/2}$ and Co $2p_{1/2}$ of Co^{2+}, respectively[10]. The peaks at 784.00 eV and 801.46 eV are the characteristic satellite peaks of Co^{2+}. In the Fe 2p spectrum, the peaks centered at 710.90 eV and 724.04 eV are attributed to Fe (III), while the peaks at 713.24 eV and 726.74 eV correspond to Fe (II)[12]. Thus, in FeCoBHT, Co exists primarily in the +2 state, while Fe is mixed of +2/+3. The XPS results further confirm the strong chemical interaction between BHT ligand and Fe and Co ions.

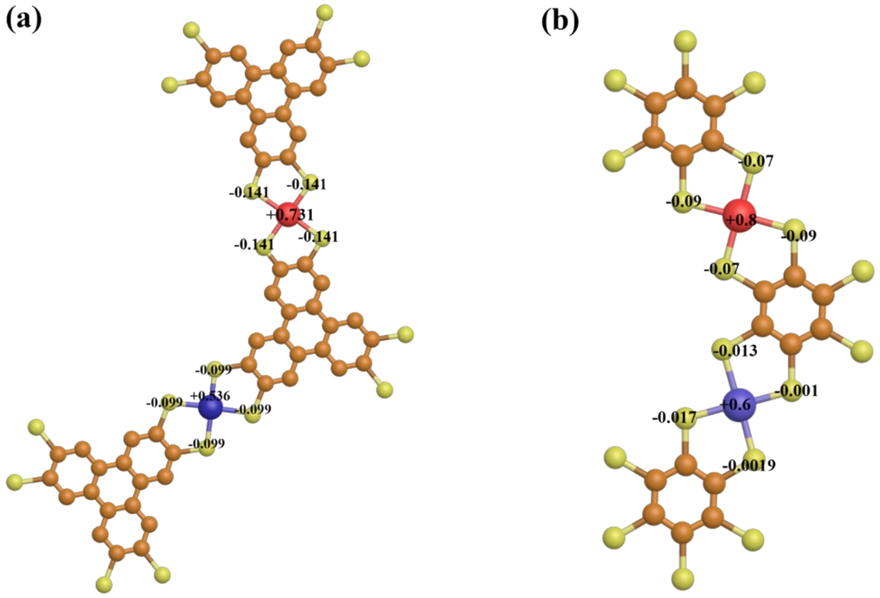

Fig. S9 Bader charge distribution of (a) FeCoTHT and (b) FeCoBHT. The color of brown, yellow, red, and blue represent C, S, Fe, and Co atoms, respectively.

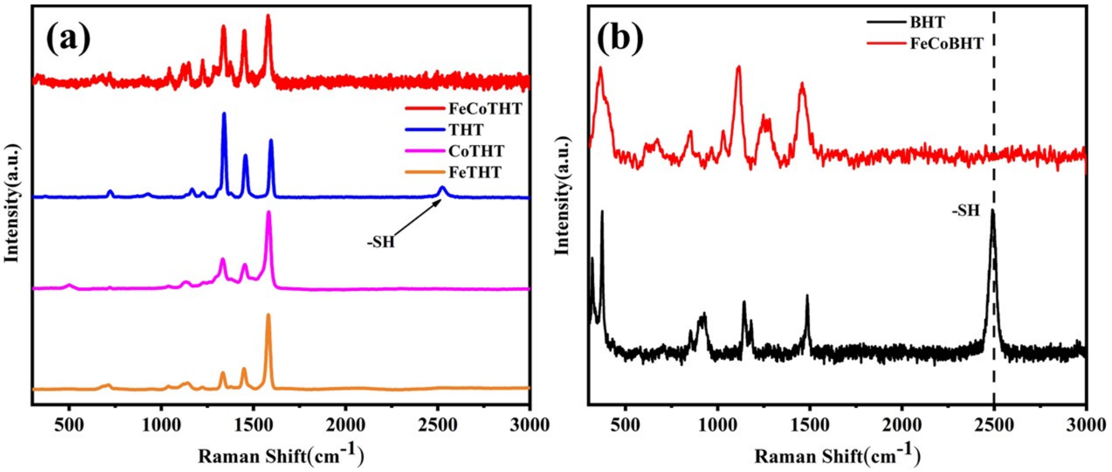

Fig. S10 Raman spectra of (a) FeCoTHT, CoTHT, FeTHT and THT; (b) FeCoBHT and BHT. The Raman spectra of FeCoTHT, CoTHT, and FeTHT exhibit similarities. When compared with the Raman spectrum of THT, the -SH peak at 2500 cm^{-1} disappears in the other three materials. The result indicates that the mercapto groups of THT were involved in the coordination reaction within FeCoTHT, CoTHT and FeTHT. A comparison of the Raman spectra of FeCoBHT and BHT reveals the disappearance of the characteristic -SH peak, indicating that the thiol group of BHT participated in the reaction of coordinating with Fe and Co ions.

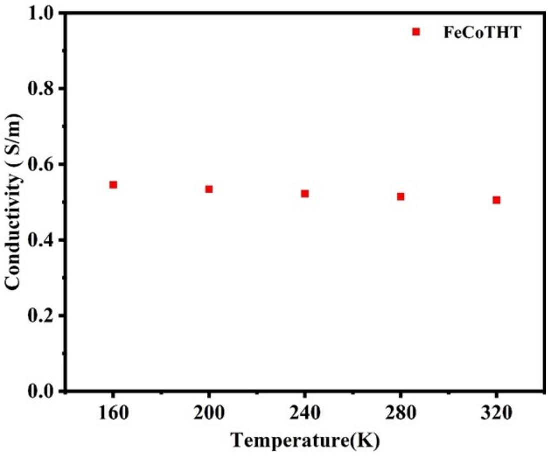

Fig. S11 Temperature dependence of the electrical conductivity of FeCoTHT.

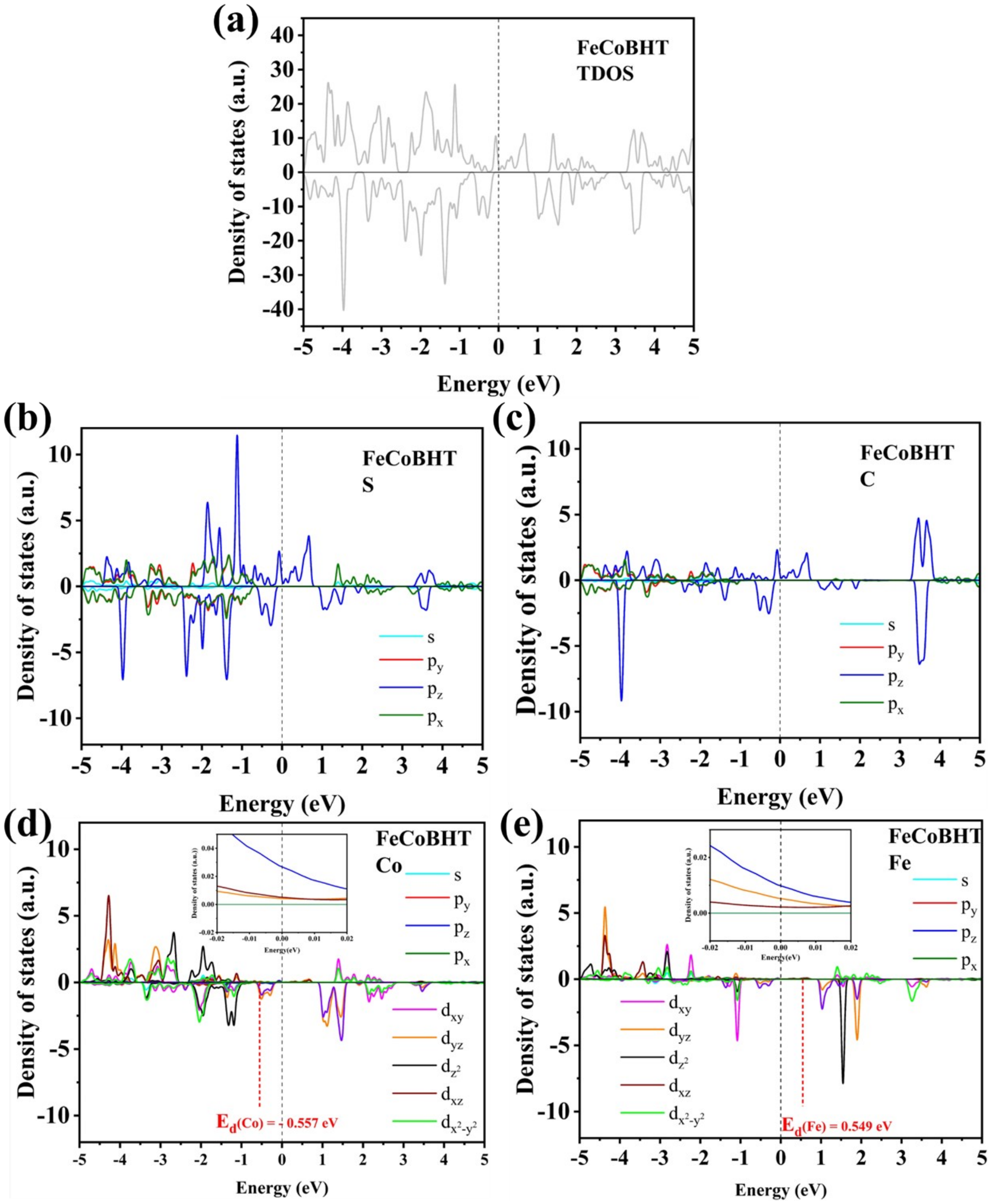

Fig. S12 (a) Total density of states (TDOS) of FeCoBHT; (b, c) partial density of states (PDOS) of S and C in FeCoBHT; (d, e) PDOS and d-band center of Fe and Co sites in FeCoBHT. The TDOS diagram for FeCoBHT shows a high local DOS near the Fermi level, indicating pronounced metallic behavior of FeCoBHT. Additionally, the DOS near the Fermi level is primarily contributed by the p_z orbitals of C and S atoms and the d_{yz}, d_{xz} and p_z orbitals of Fe and Co atoms. The results indicate that FeCoBHT exhibits pronounced π-conjugated characteristics, supporting the FeCoBHT conductive properties.

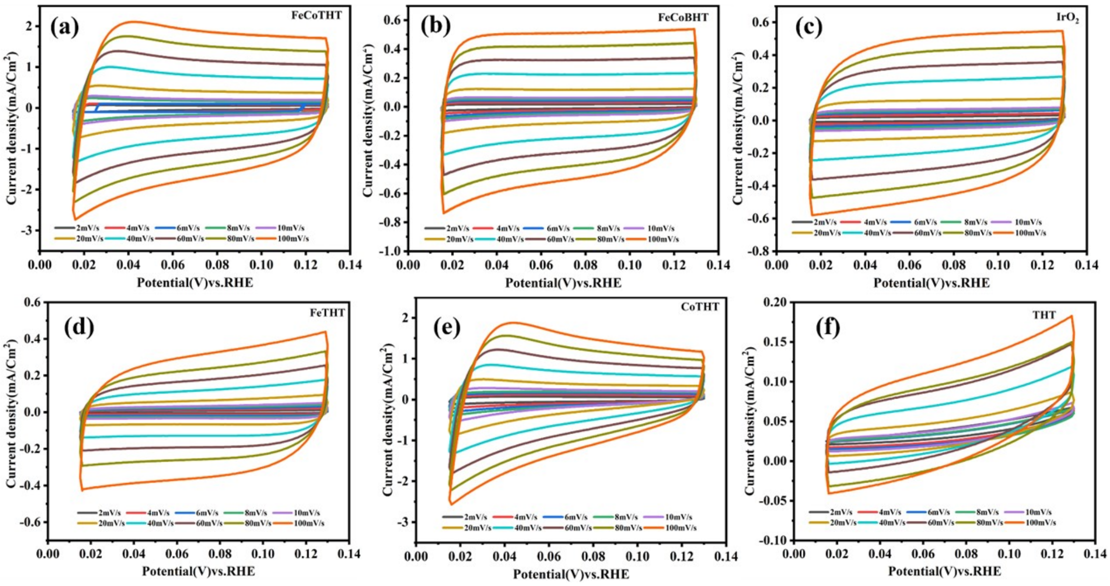

Fig. S13 Cyclic voltammograms of (a) FeCoTHT; (b) FeCoBHT; (c) IrO$_2$, (d) FeTHT, (e) CoTHT and (f) THT in the range of 1.026 - 1.141 V (vs. RHE) at different scan rates in 1.0 M KOH.

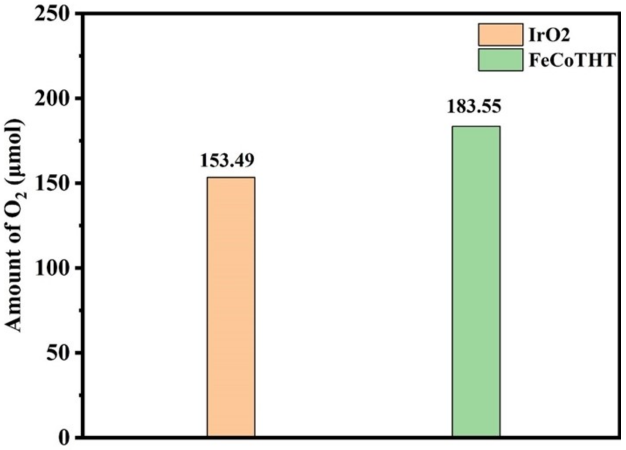

Fig. S14 Amount of O$_2$ evolved over IrO$_2$ and FeCoTHT electrodes in 60 min at a voltage of 1.7 V (vs. RHE).

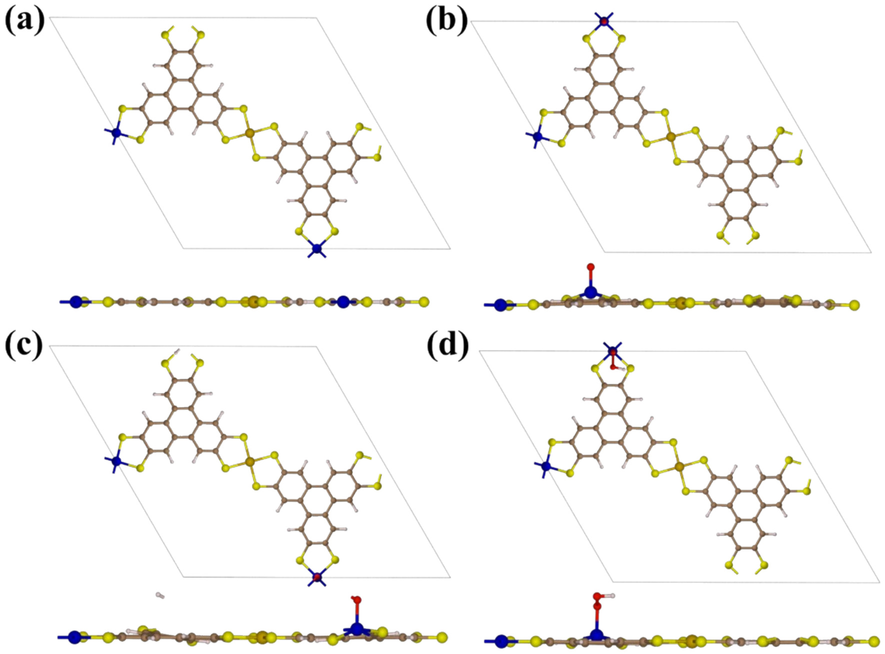

Fig. S15 Adsorption configurations of OER intermediates on the FeCoTHT surface: (a) no intermediates adsorbed; (b) *O intermediate; (c) *OH intermediate; (d) *OOH intermediate absorbed on the Co sites.

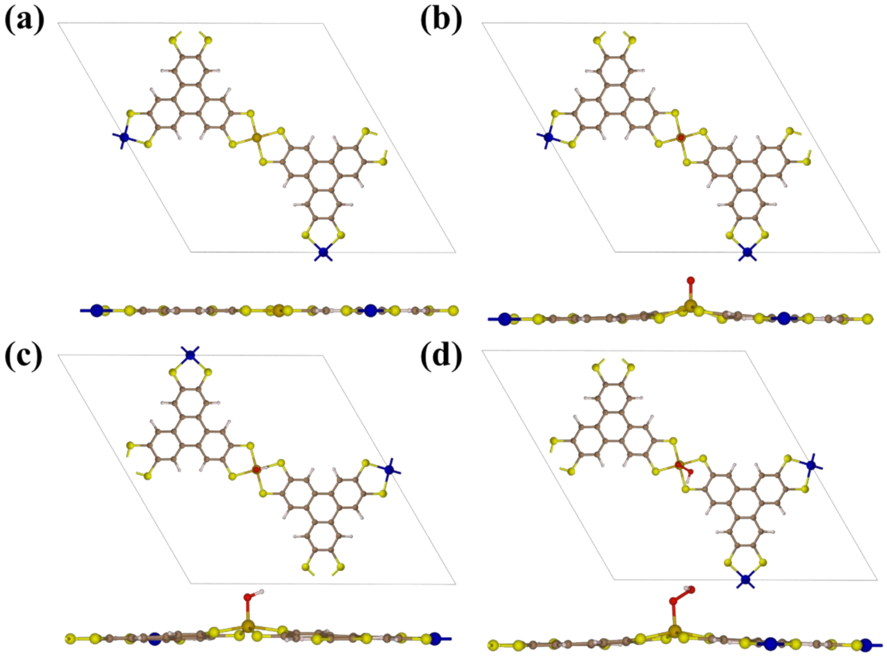

Fig. S16 Adsorption configurations of OER intermediates on the FeCoTHT surface: (a) no intermediates adsorbed; (b) *O intermediate; (c) *OH intermediate; (d) *OOH intermediate absorbed on the Fe sites.

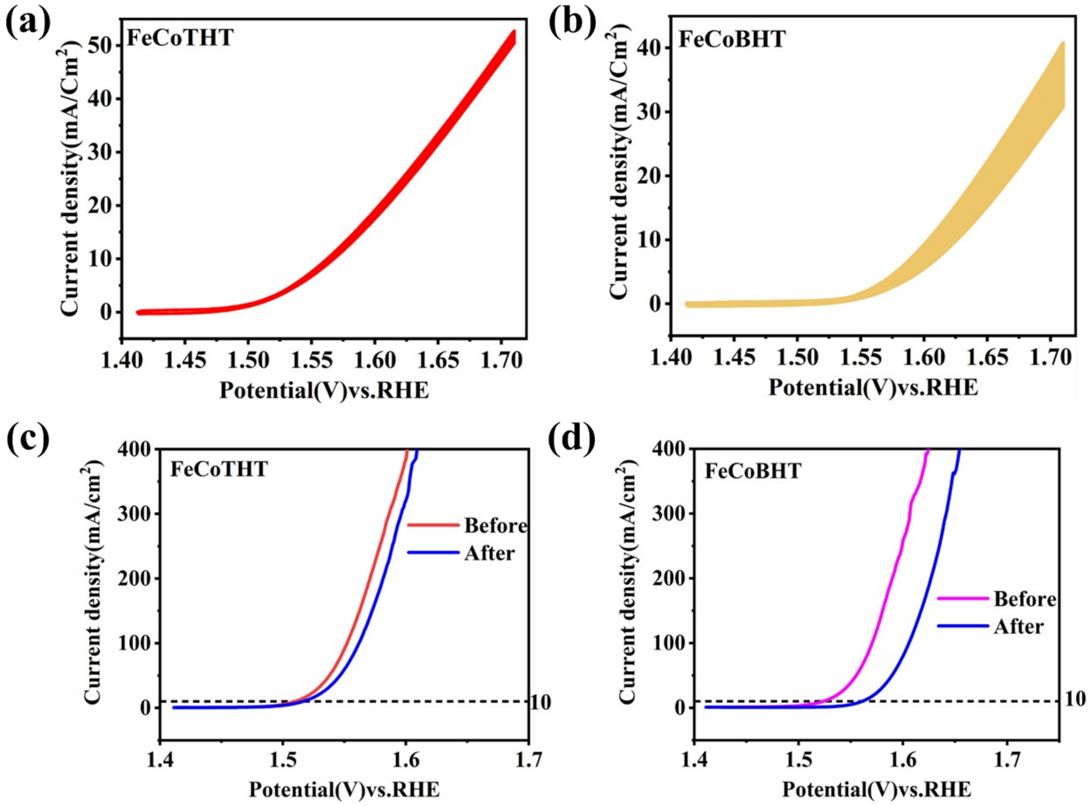

Fig. S17 CV curves of (a) FeCoTHT and (b) FeCoBHT over 2000 cycles in the voltage window of 1.4-1.7 V (vs. RHE); LSV curves of (c) FeCoTHT and (d) FeCoBHT before and after 2000 cycles of CV sweeping.

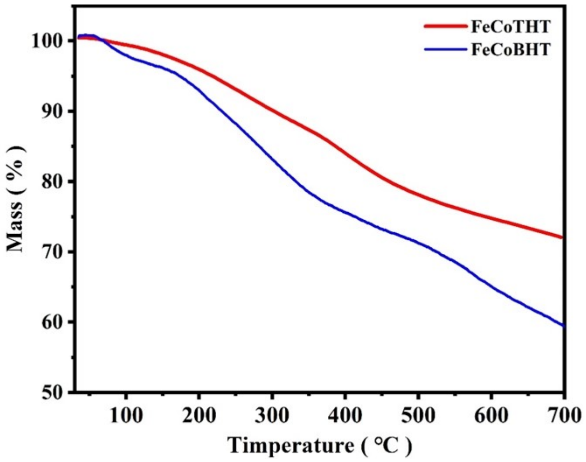

Fig. S18 Thermogravimetric analysis (TGA) curves of FeCoTHT and FeCoBHT from 75 to 700 °C.

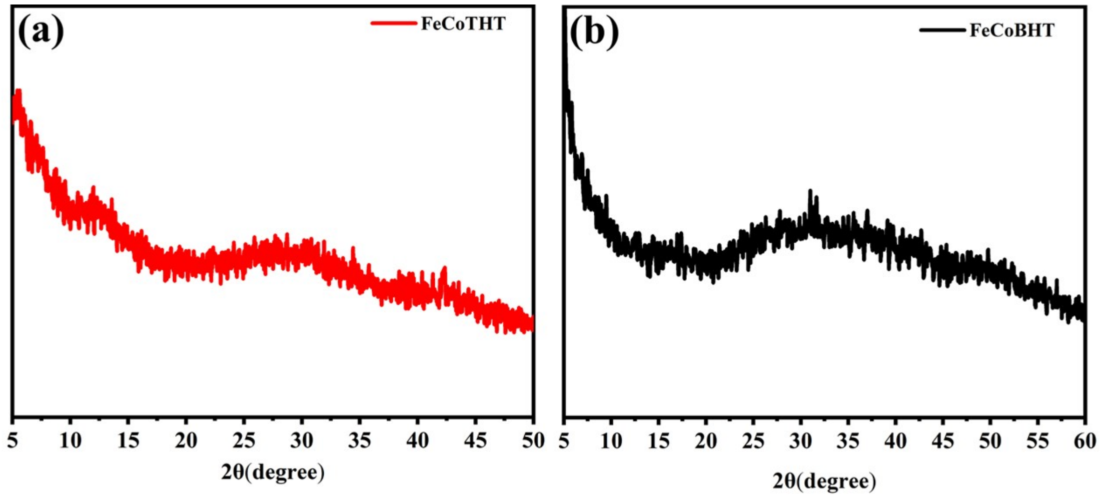

Fig. S19 XRD profiles of FeCoTHT (a) and FeCoBHT (b) after the OER.

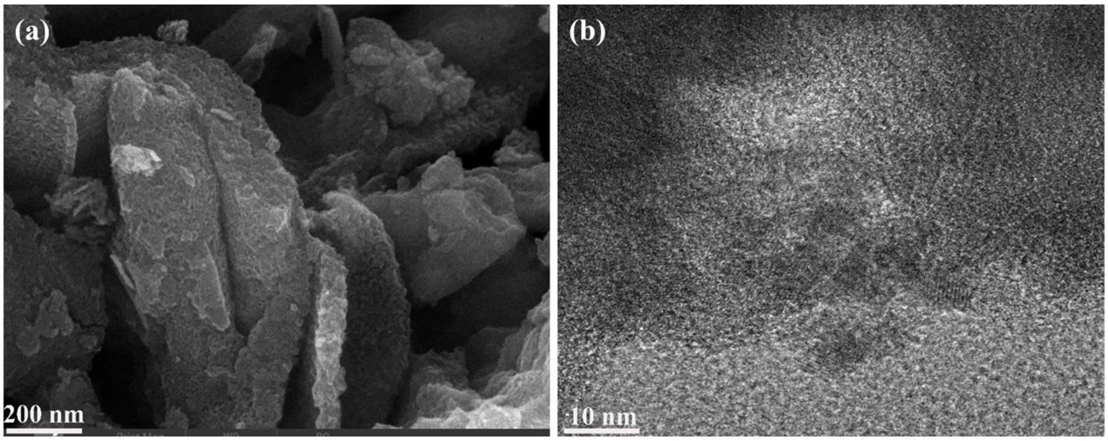

Fig. S20 (a) SEM and (b) TEM images of FeCoTHT after the OER.

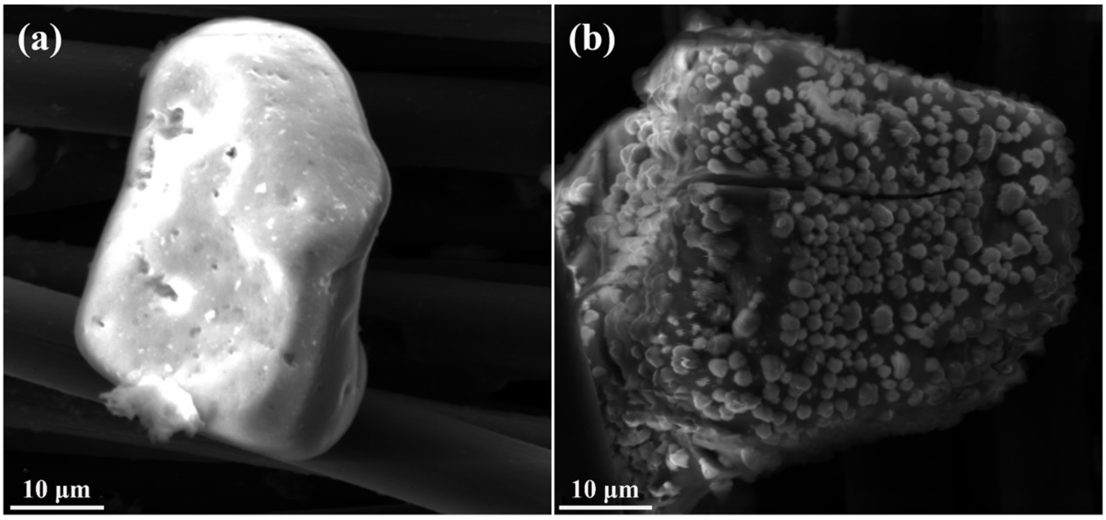

Fig. S21 SEM images of FeCoBHT before (a) and after (b) the OER.

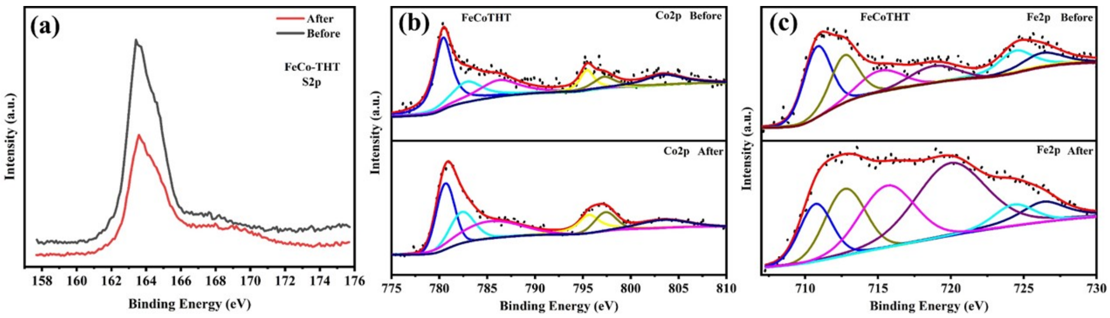

Fig. S22 XPS S 2p (a); Co 2p (b) and Fe 2p (c) spectra of FeCoTHT before and after the OER.

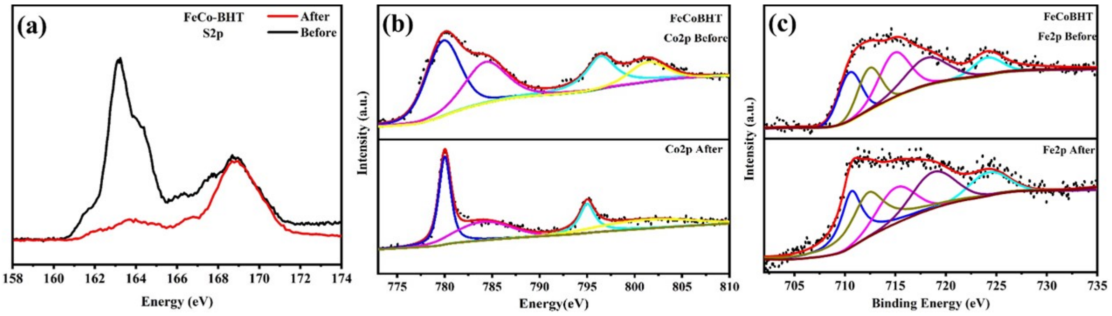

Fig. S23 XPS S 2p (a); Co 2p (b) and Fe 2p (c) spectra of FeCoBHT before and after the OER.

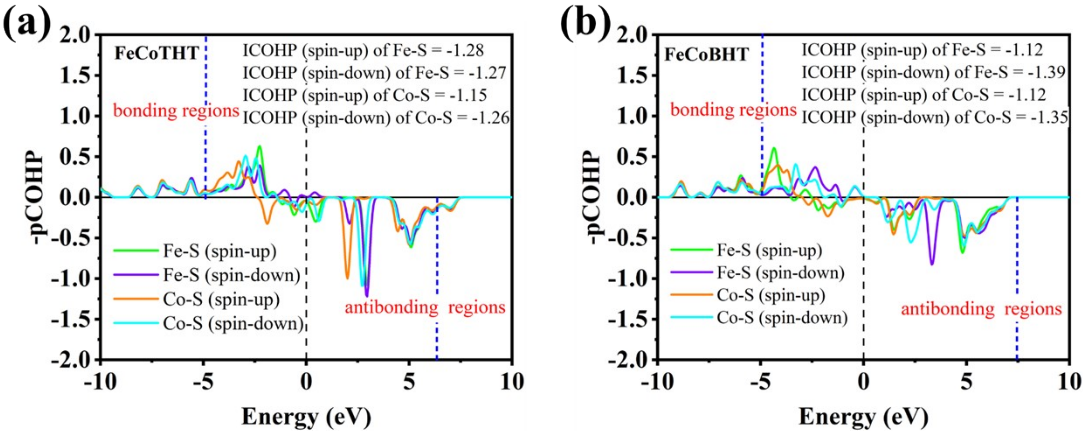

Fig. S24 Crystal orbital Hamilton population (COHP) and integrated COHP (ICOHP) analysis of FeCoTHT (a) and FeCoBHT (b).

Table S1. Elemental contents of FeCoTHT measured by ICP

Elemental	Fe	Co
Elemental content	3.0%	6.8%

Table S2. Fitting results of the EXAFS data at the Co K-edge, and Fe K-edge, where R refers to distance between absorber and backscatter atoms, CN^a the coordination numbers, σ^2 the Debye-Waller factor.

Sample	Shell	CN^a	R(Å) ^{b}	σ^2(Å^2) ^{c}
		Co K-edge		
Co foil	Co-Co	12.0	2.49±0.01	0.0063
Co_2O_3	Co-O	2.6±0.1	1.91±0.01	0.0018
	Co-Co1	2.6±0.2	2.85±0.01	0.0034
	Co-Co2	4.7±0.5	3.35±0.01	0.00652
CoO	Co–O	6.0	2.10±0.01	0.0073
	Co-Co	12.0	3.00±0.01	0.0072
CoS_2	Co-S	6.0	2.32±0.01	0.0056
FeCoTHT	Co–S	4.1±0.2	2.24±0.01	0.0065
		Fe K-edge		
Fe-foil	Fe-Fe1	8	2.47±0.01	0.0048
	Fe-Fe2	6	2.85±0.01	0.0062
FeO	Fe-O	6	2.12±0.01	0.0144
	Fe-Fe	12	3.07±0.01	0.0120
Fe_2O_3	Fe-O1	3	1.93±0.01	0.0062
	Fe-O2	3	2.09±0.01	0.0099
	Fe-Fe1	1	2.90±0.01	0.0041
	Fe-Fe2	3	2.97±0.01	0.0070
	Fe-Fe3	3	3.35±0.01	0.0070
FeS_2	Fe-S	6	2.26±0.01	0.0033
FeCoTHT	Fe-S	3.9±0.1	2.22±0.01	0.0089

Table S3. The comparison of the OER performances with different MOFs.

Catalyst	Electrolyte	η at J=10 mA cm^{-2} (mV)	Tafel slope (mV dec^{-1})	Substrate	Ref.

FeCoTHT	1.0 M KOH	253	47.61	Carbon cloth	This work
NiCo-MOF/NF	1.0 M KOH	270	35.4	Ni foam	[13]
Ni-MOF@Fe-MOF	1.0 M KOH	265	82	GC	[14]
Fe_2Ni-BPTC	1.0 M KOH	365	81.8	Carbon cloth	[15]
NiFe-BDC-0.5	1.0 M KOH	256	45.4	GC	[16]
FeCo-L_1L_2 (L_1: 2,5-dihydroxyterephthalic acid; L_2: 4,6-dihydroxyisophthalic acid)	1.0 M KOH	283	31.6	Carbon paper	[17]
TAB-TB，Co-MCOF	1.0 M KOH	268.8	80.1	RDE	[18]
$CoMn_{0.01}$	1.0 M KOH	255	66	Ni foam	[19]

Table S4. R_{ct} values of THT, FeTHT, FeCoBHT, FeCoTHT, CoTHT, IrO_2.

Sample	Rct /Ω
THT	83.15
FeTHT	6.02
FeCoBHT	0.54
FeCoTHT	0.31

CoTHT	1.23
IrO_2	0.82

References

1 J. Y. Jung, J. H. Park, Y. J. Jeong, K. H. Yang, N. K. Choi, S. H. Kim and W. J. Kim, *Korean Journal of Physiology and Pharmacology*, 2006, **10**, 289–295.

2 R. A. Vargas-Hernández, *Journal of Physical Chemistry A*, 2020, **124**, 4053–4061.

3 P. E. Blöchl, *Physical Review B*, 1994, **50**, 17953–17979.

4 K. Li, L. Luo, Y. Zhang, W. Li and Y. Hou, *ACS Applied Materials and Interfaces*, 2018, **10**, 41525–41534.

5 R. Dong, P. Han, H. Arora, M. Ballabio, M. Karakus, Z. Zhang, C. Shekhar, P. Adler, P. S. Petkov, A. Erbe, S. C. B. Mannsfeld, C. Felser, T. Heine, M. Bonn, X. Feng and E. Cánovas, *Nature Materials*, 2018, **17**, 1027–1032.

6 S. Grimme, J. Antony, S. Ehrlich and H. Krieg, *Journal of Chemical Physics*, DOI:10.1063/1.3382344.

7 J. D. Pack and H. J. Monkhorst, *Physical Review B*, 1977, **16**, 1748–1749.

8 A. Allouche, *Journal of computational chemistry*, 2012, **32**, 174–182.

9 A. H. Larsen, *Journal of Physics: Condensed Matter TOPICAL*, 2012, **29**, 1–21.

10 D. Xing, H. Wang, Z. Cui, L. Lin, Y. Liu, Y. Dai and B. Huang, *Journal of Colloid and Interface Science*, 2024, **656**, 309–319.

11 Z. Wu, D. Adekoya, X. Huang, M. J. Kiefel, J. Xie, W. Xu, Q. Zhang, D. Zhu and S. Zhang, *ACS Nano*, 2020, **14**, 12016–12026.

12 K. Ge, S. Sun, Y. Zhao, K. Yang, S. Wang, Z. Zhang, J. Cao, Y. Yang, Y. Zhang, M. Pan and L. Zhu, *Angewandte Chemie International Edition*, 2021, **60**, 12097–12102.

13 P. Thangasamy, S. Shanmuganathan and V. Subramanian, *Nanoscale Advances*, 2020, **2**, 2073–2079.

14 K. Rui, G. Zhao, Y. Chen, Y. Lin, Q. Zhou, J. Chen, J. Zhu, W. Sun, W. Huang and S. X. Dou, *Advanced Functional Materials*, 2018, **28**, 1–9.

15 X. L. Wang, L. Z. Dong, M. Qiao, Y. J. Tang, J. Liu, Y. Li, S. L. Li, J. X. Su and Y. Q. Lan, *Angewandte Chemie International Edition*, 2018, **57**, 9660–

9664.

16 D. Wang, F. Le, J. Lv, X. Yang, X. Chen, H. Yao and W. Jia, *molecules*, 2023, **28**, 1–13.

17 E. Lv, J. Yong, J. Wen, Z. Song, Y. Liu, U. Khan and J. Gao, *Energy Advances*, 2022, **1**, 641–647.

18 C. Lin, H. Ma, J. R. He, Q. Xu, M. Song, C. X. Cui, Y. Chen, C. X. Li, M. Jiao and L. Zhai, *Small*, 2024, **20**, 1–10.

19 H. Zhang, N. Sun, X. Si, Y. Zhang, F. Ding, X. Kong and Y. Sun, *Inorganic Chemistry*, 2024, **63**, 2997–3004.